Coherent electron transport in bent cylindrical surfaces

Alex Marchi,* Susanna Reggiani, and Massimo Rudan
Advanced Research Center on Electronic Systems (ARCES), and Department of Electronics (DEIS), University of Bologna, Italy

Andrea Bertoni
INFM-S3 Research Center, Modena, Italy
and Advanced Research Center on Electronic Systems (ARCES), University of Bologna, Italy
(Received 2 February 2005; published 1 July 2005)

The coherent dynamics of carriers bound to bent cylindrical surfaces is modeled by numerically solving the open-boundary Schrödinger equation recast in surface curvilinear coordinates. The effect of the surface topology on the transmission properties is addressed for bent cylinders and smooth junctions of cylinders with different radii. It is shown that, where the curvature changes sharply, quantum interference phenomena are induced, leading to an oscillatory behavior of the transmission coefficient as a function of the geometrical parameters. The spectra of bound states are also computed. The analysis has been carried out using the geometrical and physical parameters of carbon nanotubes, whose topology can be modeled, in many significant cases, using the presented approach.

DOI: 10.1103/PhysRevB.72.035403 PACS number(s): 73.20.−r, 02.40.−k, 73.23.Ad, 73.63.Fg

I. INTRODUCTION

The technological advances in nanoelectronic-device fabrication and the search for the post-complementary metal-oxide-semiconductor device family have recently led to considering a number of systems in which the carrier dynamics is confined in one or two directions[1–3] as a possible basis for the emerging nanoelectronics. If the energy scale of the quantum states in the confining direction is substantially larger than the mean kinetic energy of the carrier, the quantized direction can safely be neglected when computing the carrier motion: this naturally implies the reduction of the number of the spatial variables of the problem, with a substantial simplification in the physical modeling. When the subspace of $\mathbb{R}^3$ where the particle motion takes place is curved, the reduction in the number of variables is still possible through the limiting procedure described by da Costa.[4] Such an approach has successfully been applied, for example, to the band-structure calculation of real systems[5] and to the determination of localized surface states in deformed quantum wires.[6] Furthermore, experimental evidence of localized states induced by the topology of highly oxidized porous silicon samples have been presented.[7,8] Although the resulting equation of motion is considerably more complicated than the standard Schrödinger equation, the computational burden of the numerical solution is smaller, and the ruling out of the confining direction allows for a direct numerical simulation of cases that would be unaffordable for a full three-dimensional (3D) approach. Furthermore, since the first step toward the solution is analytical, some physical insight can be gained by inspecting the effective potential raising from the curvature of the surface, as will be shown in the following.

In this work we analyze the coherent dynamics of a single carrier bound to a bent cylindrical surface, possibly with a variable diameter. The examples we investigate have a general validity and can be thought of as models for the ballistic surface transport of a number of realistic cylindrical nanosystems.[9] Here we take as a reference a semiconducting carbon nanotube (CNT)[10,11] and use its physical parameters in the simulations. Moreover, we consider geometrical parameters (cylinder diameters and bending radii) that are compatible with semiconducting CNTs.

We stress that our approach uses an effective mass and is based on the well-known envelope-function model, whose validity is limited to the case of a perfectly periodic atomic configuration, like a 3D crystal or a straight CNT. In the case of bent CNTs or junctions between CNTs with different chiralities, the envelope-function approach can still be used as an approximation, provided that two effects are taken into account, namely the local change in the electronic properties[12,13] and the geometrical deformation of the structure.

The local change in the electronic properties can be incorporated into the model by means of a position-dependent effective mass, as usually made when dealing with semiconductor heterostructures, or by means of a more sophisticated position-dependent band structure.[14] Such an issue will not be addressed in this paper, and proper references will be made to the existing literature when necessary. In particular, the concept of effective mass will be used in the examples given later, in which the values of the effective masses are taken from Refs. 15 and 16.

The subject of the present work is the effect of the geometrical deformation of the structure, which is of a purely topological origin. The description of the dynamics of a particle bound to a two-dimensional (2D) surface curved within the 3D real space is given in Sec. II, where the particular case of a cylindrical surface will also be treated in detail. In Secs. III–V three specific cases, namely, bent-cylindrical surfaces, and symmetric- and asymmetric-cylindrical junctions are addressed, respectively. For each case, the corresponding surface parametrization is given first, along with the effective potential originated by the topology under study. Then, the transmission coefficient for different geometrical parameters is calculated to describe the coherent-transport properties of

the investigated structure. In Sec. VI, the energy spectra of localized states arising in some of the structures indicated above are calculated and discussed. Finally, the conclusions are drawn in Sec. VII.

II. QUANTUM DYNAMICS OF A PARTICLE CONSTRAINED ON A SURFACE

A 2D regular surface S curved within the 3D real space is described by the parametric equation $\mathbf{r}=[x(q_1,q_2), y(q_1,q_2),z(q_1,q_2)]$, with q_1 and q_2 the curvilinear coordinates over S. It is useful to introduce also the q_3 coordinate representing the distance from S along the direction normal to it. The unit vector of such direction is $\mathbf{n}/|\mathbf{n}|$, with $\mathbf{n}(q_1,q_2)=(\partial\mathbf{r}/\partial q_1)\wedge(\partial\mathbf{r}/\partial q_2)$. We briefly outline here the procedure that yields the equation of motion for a particle bound to S. First, a confining potential $V_c(q_1,q_2,q_3)$ is introduced which, after a proper limiting procedure,[4] becomes $V_c=0$ if $q_3=0$ and $V_c=\infty$ otherwise. This separates the q_3 dependence in the particle Hamiltonian expressed in the new coordinates q_1, q_2, q_3. The part of the Hamiltonian depending on q_1, q_2 takes the form:

$$\mathcal{H}=-\frac{\hbar^2}{2m}\sum_{i,j=1}^{2}\frac{1}{\sqrt{G}}\frac{\partial}{\partial q_i}\left[\sqrt{G}(\mathbf{G}^{-1})_{ij}\frac{\partial}{\partial q_j}\right]-\frac{\hbar^2}{2m}(M^2-K)+V_{\text{ext}}, \tag{1}$$

where m is the particle mass, the 2×2 matrix $\mathbf{G}$ the first fundamental form[17] of S, with elements $G_{ij}(q_1,q_2)=(\partial\mathbf{r}/\partial q_i)\cdot(\partial\mathbf{r}/\partial q_j)$, $G>0$ the determinant of $\mathbf{G}$, $M(q_1,q_2)$ and $K(q_1,q_2)$ the mean and Gaussian curvatures of S, respectively, and $V_{\text{ext}}(q_1,q_2)$ an externally applied potential. By indicating with $H_{ij}(q_1,q_2)=(\partial^2\mathbf{r}/\partial q_i\partial q_j)\cdot\mathbf{n}/|\mathbf{n}|$ the coefficients of the second fundamental form,[17] M and K read

$$M=\frac{1}{2G}(G_{11}H_{22}+G_{22}H_{11}-2G_{12}H_{12}),$$

$$K=\frac{1}{G}(H_{11}H_{22}-H_{12}H_{21}). \tag{2}$$

For a given point P of S, each plane containing the vector $\mathbf{n}$ normal to S at P intersects the surface along a curve. Let $\mathcal{C}$ be the curvature of such curve at P, and let $\mathcal{C}_m$ and $\mathcal{C}_M$ be the minimum and maximum of $\mathcal{C}$ as the plane rotates by π around $\mathbf{n}$. It is well-known[17] that $M=(\mathcal{C}_m+\mathcal{C}_M)/2$ and $K=\mathcal{C}_m\mathcal{C}_M$. As a consequence, $M^2\geqslant K$. In particular, for a cylindrical surface $M=\mathcal{C}_M$ and $K=0$, while for a saddle point $K<0$ and, if $|\mathcal{C}_m|=|\mathcal{C}_M|$, $M=0$. The mean and Gaussian curvatures contribute to the Hamiltonian $\mathcal{H}$ of Eq. (1) to form an effective-potential term $U(q_1,q_2)=-\hbar^2(M^2-K)/(2m)\leqslant0$. The kinetic term in Eq. (1) contains mixed second-order derivatives and first-order derivatives, both with nonconstant coefficients. The reduction of the computational burden, due to transforming the problem from three to two dimensions, largely compensates the complicacy of using curvilinear coordinates, which is actually a minor drawback in the numerics.

The remaining part of this section will be devoted to providing the necessary details about the cylindrical surface, which is the building block of the analysis to follow. Using the symbol s instead of q_1, its parametrization is given by

$$x=\rho\cos(s/\rho),$$

$$y=q_2,$$

$$z=\rho\sin(s/\rho), \tag{3}$$

where ρ is the cylinder's radius. It follows

$$\mathbf{G}=\begin{pmatrix}1&0\\0&1\end{pmatrix},\quad \mathbf{H}=\begin{pmatrix}1/\rho&0\\0&0\end{pmatrix}, \tag{4}$$

$$M=\frac{1}{2\rho},\quad K=0. \tag{5}$$

Finally, its Hamiltonian $\mathcal{H}_{\text{cyl}}$ reads

$$\mathcal{H}_{\text{cyl}}=-\frac{\hbar^2}{2m}\left(\frac{\partial^2}{\partial s^2}+\frac{\partial^2}{\partial q_2^2}\right)-\frac{\hbar^2}{8m\rho^2}+V_{\text{ext}}. \tag{6}$$

Note that in this case the effective potential U is a negative constant and does not play any role in the particle dynamics. If no external potential is applied ($V_{\text{ext}}=0$) the Hamiltonian (6) splits into the angular and axial terms. The solution is standard and is made by the product of a free-particle term in the axial direction q_2 and a periodical term in the angular coordinate s.

III. BENT CYLINDRICAL SURFACES

The first nontrivial case we considered is a bent cylindrical surface S_{bc} described by the following parametrization:

$$x=[R+\rho\cos(s/\rho)]\cos(q_2/R),$$

$$y=[R+\rho\cos(s/\rho)]\sin(q_2/R),$$

$$z=\rho\sin(s/\rho), \tag{7}$$

where ρ is the radius of the cylinder, R the curvature radius of the cylinder's axis, and s, q_2 the curvilinear coordinates. The surface S_{bc} is shown in Fig. 1 together with two short straight cylinders connected at the two ends. The first and second fundamental forms of it are

$$\mathbf{G}=\begin{pmatrix}1&0\\0&[R+\rho\cos(s/\rho)]^2/R^2\end{pmatrix}, \tag{8}$$

$$\mathbf{H}=\begin{pmatrix}1/\rho&0\\0&\cos(s/\rho)[R+\rho\cos(s/\rho)]/R^2\end{pmatrix}. \tag{9}$$

From Eq. (2) one finds for the mean and Gaussian curvature:

$$M=\frac{R+2\rho\cos(s/\rho)}{2\rho[R+\rho\cos(s/\rho)]}, \tag{10}$$

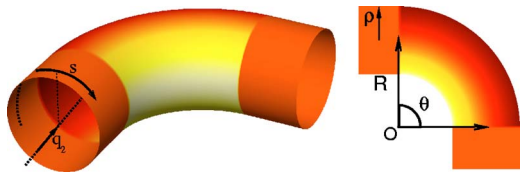

FIG. 1. (Color online) Bent cylindrical surface S_{bc} with two straight cylinders at the two ends. Left: the gray intensity shows the effective potential U originating from the curvature of the surface. The curvilinear coordinates s, q_2 are indicated. The surface curvature depends on s: the maximum curvature is reached at the "inner" points. Right: top view of the structure. The curvature radius R and the curvature angle θ are shown along with the radius ρ of the cylinders. In the example shown it is $R=4$ nm and $\rho=1.55$ nm.

$$K = \frac{\cos(s/\rho)}{\rho[R + \rho\cos(s/\rho)]}. \tag{11}$$

Finally, the Hamiltonian (1) becomes

$$\mathcal{H}_{bc} = -\frac{\hbar^2}{2m}\left\{\frac{\partial^2}{\partial s^2} - \frac{\sin(s/\rho)}{R+\rho\cos(s/\rho)}\frac{\partial}{\partial s} + \frac{R^2}{[R+\rho\cos(s/\rho)]^2}\frac{\partial^2}{\partial q_2^2}\right\} - \frac{\hbar^2 R^2}{8m\rho^2[R+\rho\cos(s/\rho)]^2} + V_{ext}. \tag{12}$$

As expected, the straight-cylinder Hamiltonian is recovered from Eq. (12) in the limiting case when $R\to\infty$. In the following, the case $V_{ext}=0$ will be considered for the sake of simplicity. From the numerical standpoint, the extension to the case $V_{ext}\neq 0$ is straightforward.

The effective potential $U(s,q_2)$ is shown in Fig. 2. At the two ends, where the cylinder is straight, the potential $U=-\hbar^2/(8m\rho^2)$ is constant, which explains the discontinuity at the connections with S_{bc}. Within S_{bc}, the maximum and minimum of U correspond to the least- and most-curved parts of S_{bc}, respectively. The constant value $U=-\hbar^2/(8m\rho^2)$ in the straight cylinders is always between the above values, this leading to a potential well and a potential barrier along the axial direction at different angular positions. As observed in Fig. 1, the surface curvature depends on the angular coordinate: in particular, the maximum curvature is reached at the "inner" points, nearest to the point O visible in Fig. 1, and the minimum curvature is reached at the "outer" points.

The depths of the potential well and barrier mentioned above depend on both the cylinder radius ρ and on the curvature radius R. In Fig. 3(a) the difference ΔU between the maximum and minimum values of U is reported as a function of R for two different cylinder radii: it represents the overall variation in the effective potential U that a carrier experiences while propagating along the surface. The asymptotic values of ΔU are zero for $R\to\infty$ (straight cylinder) and ∞ for $R\to\rho$. The crossing of the curves indicates that for small curvature radii R the potential energy is steeper in the larger cylinder than in the smaller one, while at larger R this condition is inverted. This has a consequence on the transmission coefficient, as shown later. The corresponding potential cutlines at $q_2=4$ nm are reported in Figs. 3(b) and 3(c) for $R=2$ and 3 nm, respectively, showing the different behavior of the effective potential before and after the crossing point of the curves.

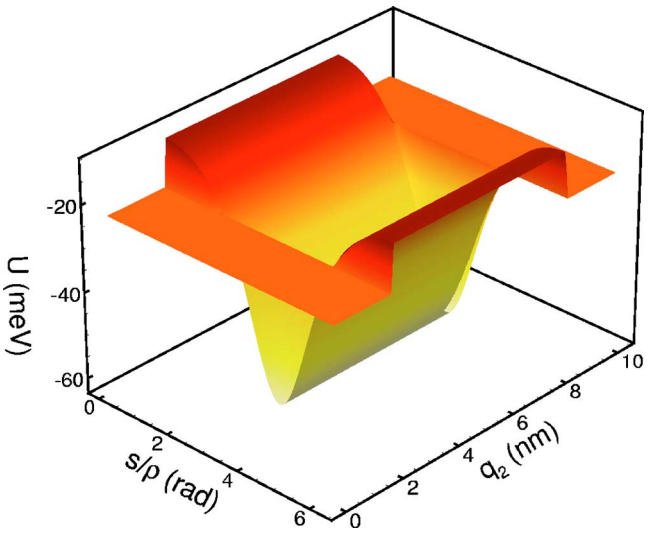

FIG. 2. (Color online) 3D plot of the effective potential U of S_{bc} as a function of the curvilinear coordinates s, q_2. The origin of s is placed at the outer points with respect to the point O visible in Fig. 1. As $\rho=1.55$ nm, the range of s is $2\pi\rho\simeq 9.74$ nm. U is negative on the whole domain S_{bc} (the gray intensity corresponds to that used in Fig. 1). Due to Eq. (6) a straight cylindrical surface has $U=-\hbar^2/(8m\rho^2)$, which explains the discontinuity at the connections between S_{bc} and the straight cylinders at the two ends.

The scattering states of the Hamiltonian (12) that contains the effective potential U described so far, have been calculated by numerically solving the time-independent Schrödinger equation $\mathcal{H}_{bc}\psi=E\psi$ with $V_{ext}=0$. The quantum-transmitting boundary method[18] has been used for the open-boundary conditions in the 2D domain (s,q_2). Specifically, the open boundaries of the domain correspond to the connections between the straight cylinders and S_{bc}. As in the straight cylinders the Hamiltonian is separable in the longitudinal and angular directions, the boundary conditions are built as a linear combination of functions

$$\phi_B = \exp(iP_l q_2/\hbar)\exp(ins/\rho), \quad P_l = \sqrt{2mE_l}, \tag{13}$$

where the first term is a plane wave of longitudinal energy $E_l>0$, and the second one is the nth eigenstate of the normal section of the cylinder, $n=0,1,\ldots$. The total energy of an electron injected in a specific angular eigenstate n is given by $E=E_l+(n^2\hbar^2)/(2m\rho^2)+U_{in}$, where U_{in} is the constant curvature potential in the injection cylinder. In the calculations of the transmission coefficient shown below, the longitudinal energy of the injected carriers E_l has been sampled from 0.1 to 10 meV, while the ground state $n=0$ has been taken for the angular component.

The transmission coefficient for a number of bent cylinders is shown in Fig. 4. Two different radii have been taken into account, namely, $\rho=0.397$ and 1.55 nm, corresponding to a (10,0) and a (25,20) CNT, respectively. Both CNTs are semiconductors and have one absolute minimum in the first branch of the conduction band. In the analysis that follows,

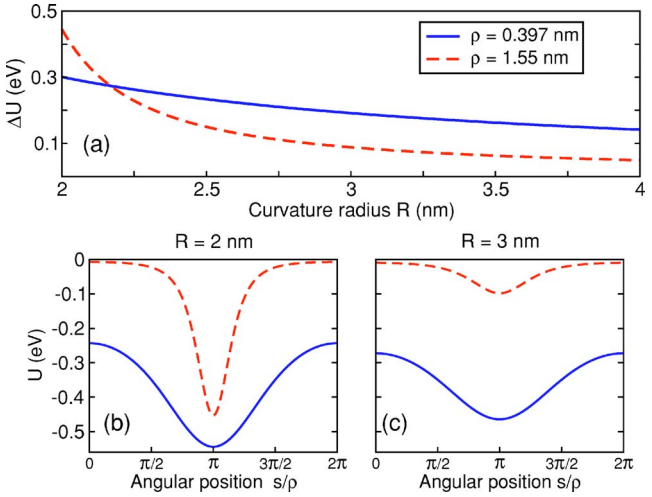

FIG. 3. (Color online) (a) Difference ΔU between the maximum and minimum of the curvature potential, as a function of the curvature radius R, for two bent cylinders with radii ρ=0.397 and 1.55 nm, respectively. (b) and (c) Potential energy cutlines (see Fig. 2) at q_2=4 nm as a function of the angular position for two different R values, before and after the crossing point of the curves in (a). For R=2 nm the curvature potential in the smaller cylinder (solid line) is smoother than that in the larger one (dashed line). The opposite occurs for R=3 nm.

the parabolic-band approximation is adopted for both CNTs, this yielding the effective-mass model for the charge transport. As the particle is constrained on a surface, the effective-mass tensor has two components. The component m_q related to the longitudinal motion, namely, along the q_2 coordinate, has been determined from an *ab initio* band calculation using the SIESTA code.[19,20] The component m_s of the effective-mass tensor related to the angular motion, namely, to the s coordinate, has purposedly been taken equal to m_q. In fact, the object of the investigation is that of determining the effect of the topology on the particle's dynamics, which should not be obscured by numerical differences in the coefficients. The common value of the two masses will still be called m. It is worth noting that, if the quantitative difference between the two mass components were taken in to account, the Hamiltonian (1) and those deriving from it should be modified accordingly.

Letting m=0.173m_e, with m_e the free electron mass, the transmission coefficient T has been calculated from Eq. (12) for each cylinder radius ρ, using three different curvature angles $\theta=\pi/3, \pi/2, 2\pi/3$ and three curvature radii R=2, 3, 4 nm. As the injection energy becomes higher, T increases monotonically and, for curvature radii that are substantially higher than ρ (e.g., R=4 nm as shown by the dotted curves in Fig. 4), it exceeds 0.8 for injection energies larger than 4 meV. Note that, when the decrease in the curvature radius R makes the latter to approach ρ (solid lines R=2 nm of the case ρ=1.55 nm), the transmission coefficient strongly decreases. As observed above, this is due to the curvature sharpness and, consequently, to the corresponding steeper effective potential U already described in Fig. 3, leading to a high reflected component of the incoming wave function. As a final remark, we note that T increases with a decreasing

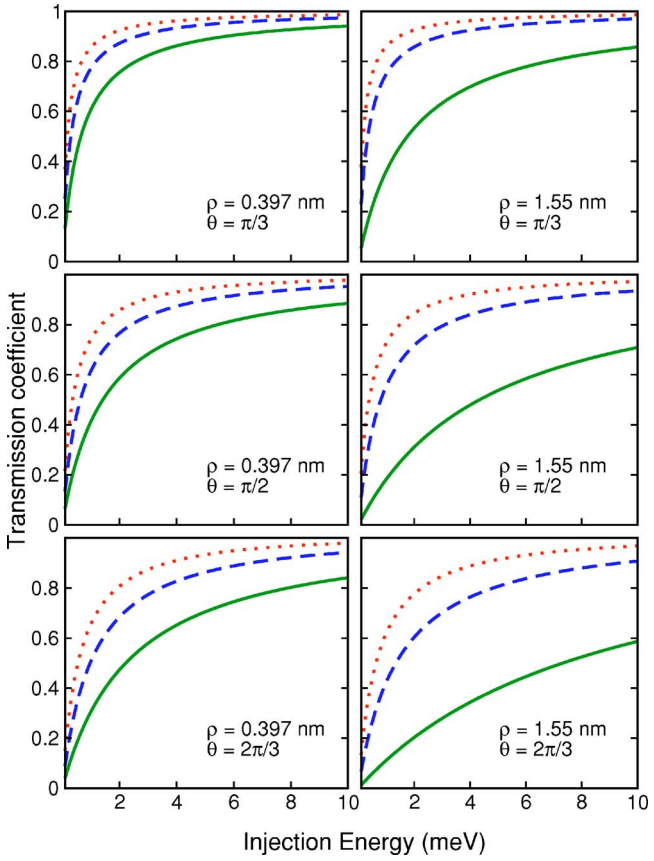

FIG. 4. (Color online) Transmission coefficient as a function of the incoming-carrier energy for two bent cylindrical surfaces with radii ρ=0.397 nm (left column) and ρ=1.55 nm (right column). Three curvature radii R=2 nm (solid line), R=3 nm (dashed line), and R=4 nm (dotted line) and three curvature angles $\theta=\pi/3$ (top), $\theta=\pi/2$, (middle), and $\theta=2\pi/3$ (bottom) are considered. The ground eigenstate n=0 is taken for the angular component of the incoming-electron wave function (see text), so that the incoming-carrier energy turns out to be $E(n=0)$.

curvature angle θ: in this case the shape of U is unaffected in the angular direction, while its extension in the longitudinal direction is proportional to θ. For larger curvature angles this leads to a wider region where the curvature potential is effective.

IV. CYLINDRICAL JUNCTIONS WITH AXIAL SYMMETRY

The parametrization of a symmetric cylindrical junction S_{scj} is given by

$$x = \rho(q_2)\cos\phi,$$

$$y = q_2,$$

$$z = \rho(q_2)\sin\phi, \tag{14}$$

where $\rho(q_2)$ is the q_2-dependent radius of the cylinder and (ϕ, q_2) are the curvilinear coordinates of S_{scj}. Two different geometries have been studied, corresponding to a single and

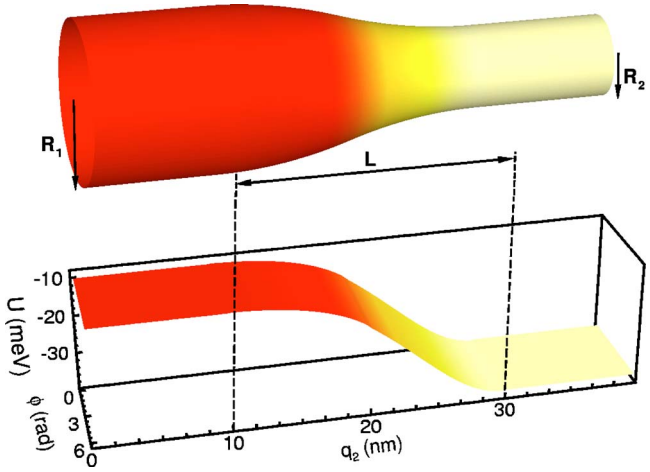

FIG. 5. (Color online) Single junction. Top: 3D representation of the surface S_{scj}. The gray intensity shows the effective potential U. Bottom: effective potential as a function of the curvilinear coordinates (ϕ, q_2) as given by Eq. (20). The potential U resembles a smoothed potential step and, due to cylindrical symmetry, is independent of the angular coordinate ϕ.

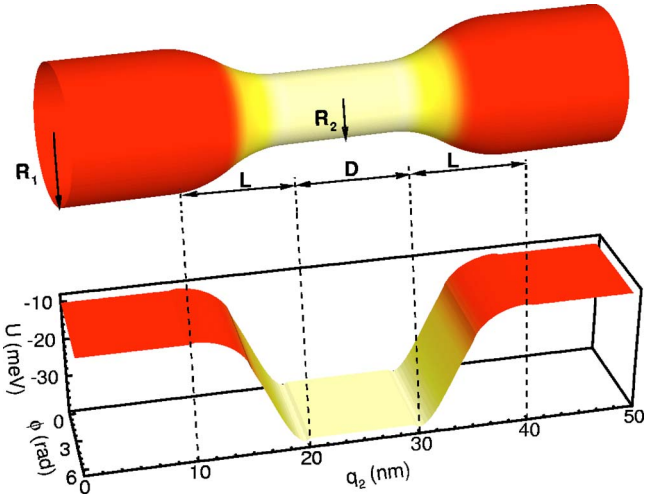

FIG. 6. (Color online) Double junction. Top: 3D representation of the surface S_{scj}. The gray intensity shows the effective potential U. Bottom: effective potential as a function of the curvilinear coordinates. The potential U resembles a smoothed potential well and is independent of the angular coordinate ϕ.

double junction (see top of Figs. 5 and 6, respectively). In order to realize a smooth transition between the two cylinders, the shape of $\rho(q_2)$ has been modeled with a five degree polynomial, which is the lowest-order polynomial that guarantees a $\mathcal{C}^2$ regularity of the surface:

$$\rho(q_2) = R_1 + (R_2 - R_1)\left[6\left(\frac{q_2}{L}\right)^5 - 15\left(\frac{q_2}{L}\right)^4 + 10\left(\frac{q_2}{L}\right)^3\right], \tag{15}$$

where R_1 and R_2 are the radii indicated in Figs. 5 and 6, and L is the length of the connecting region. The first and second fundamental forms for S_{scj} are

$$\mathbf{G} = \begin{pmatrix} \rho(q_2)^2 & 0 \\ 0 & 1 + \rho'(q_2)^2 \end{pmatrix}, \tag{16}$$

$$\mathbf{H} = \frac{1}{\sqrt{1 + \rho'(q_2)^2}} \begin{pmatrix} \rho(q_2) & 0 \\ 0 & -\rho''(q_2) \end{pmatrix}, \tag{17}$$

where the single- and double-prime superscripts indicate the first- and second-order derivatives. By using Eq. (2), one finds

$$M = \frac{1 + \{\rho'(q_2)\}^2 - \rho(q_2)\rho''(q_2)}{2\rho(q_2)[1 + \{\rho'(q_2)\}^2]^{3/2}}, \tag{18}$$

$$K = -\frac{\rho''(q_2)}{\rho(q_2)[1 + \{\rho'(q_2)\}^2]^2}. \tag{19}$$

In this case the effective potential is

$$U(q_2) = -\frac{\hbar^2}{8m}\frac{[1 + \{\rho'(q_2)\}^2 + \rho(q_2)\rho''(q_2)]^2}{\{\rho(q_2)\}^2[1 + \{\rho'(q_2)\}^2]^3}. \tag{20}$$

Finally, the Hamiltonian $\mathcal{H}_{\mathrm{scj}}$ for the symmetric cylindrical junction reads

$$\mathcal{H}_{\mathrm{scj}} = -\frac{\hbar^2}{2m}\left[\frac{G_{22}}{G}\frac{\partial^2}{\partial\phi^2} + \frac{G_{11}}{G}\frac{\partial^2}{\partial q_2^2} + \frac{1}{\sqrt{G}}\frac{\partial}{\partial q_2}\left(\frac{G_{11}}{\sqrt{G}}\right)\frac{\partial}{\partial q_2}\right] + U. \tag{21}$$

For a constant ρ the expressions (18) and (19) reduce to Eq. (5), and Eq. (21) reduces to Eq. (6). The effective potential (20) is shown in Fig. 5 for the single-junction case and in Fig. 6 for the double-junction case: thanks to the cylindrical symmetry of the junction, U depends on the q_2 coordinate only. As a consequence, in order to investigate the scattering states of the Hamiltonian $\mathcal{H}_{\mathrm{scj}}$, one separates the corresponding time-independent Schrödinger equation into the following 1D equations:

$$\Phi'' + A\Phi = 0, \tag{22}$$

$$\Upsilon'' + F(q_2)\Upsilon' + G(q_2)\{(2m/\hbar^2)[E - U(q_2)] - A\rho^{-2}(q_2)\}\Upsilon = 0, \tag{23}$$

where $\Phi(\phi)$ and $\Upsilon(q_2)$ are the angular and axial eigenfunctions, respectively, the eigenvalue A of Eq. (22) is the separation constant, and E is the total energy. Due to separation, the latter is the sum of the injection part E_l and of the angular part $\hbar^2 A/[2m\{\rho(q_2)\}^2]$. The coefficients of Eqs. (22) and (23) read

$$F(q_2) = \rho^{-1}\rho'[1 - \rho\rho''(1 + (\rho')^2)^{-1}], \tag{24}$$

$$G(q_2) = 1 + (\rho')^2. \tag{25}$$

Equation (22) is solved with periodic boundary conditions while Eq. (23) is solved numerically with open boundary conditions.[18] As in the case of the bent cylindrical surface, the results are shown for an electron injected in the ground state $A=0$. A number of cases have been investigated, with different values of the geometrical parameters, both for the single and double junction: the few reported below are rep-

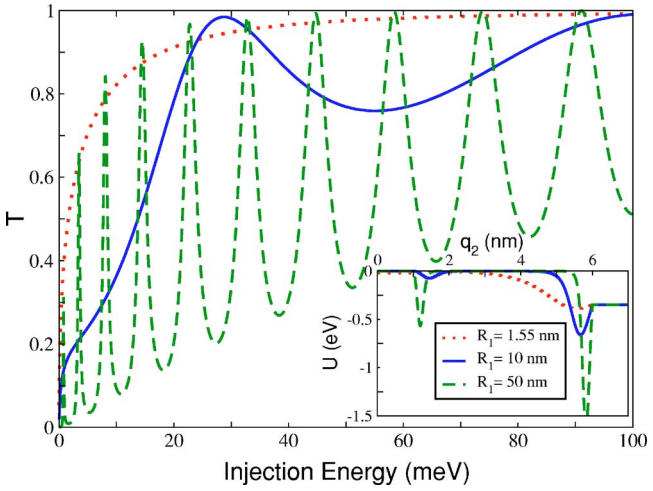

FIG. 7. (Color online) Transmission coefficient T for three single junctions as a function of the injection energy E_l. The radius of the outgoing cylinder and the length of the connecting region are fixed, namely $R_2=0.397$ nm and $L=5$ nm, while three different values $R_1=1.55$ nm (dotted curve), $R_1=10$ nm (solid curve), and $R_1=50$ nm (dashed curve) are considered for the radius of the cylinder into which the electron is injected. Inset: effective potential (20) for the three junctions described above. The two narrow wells at the junction ends ($q_2=1$ nm and $q_2=6$ nm) are more pronounced at larger R_1/R_2, corresponding to a steeper curvature.

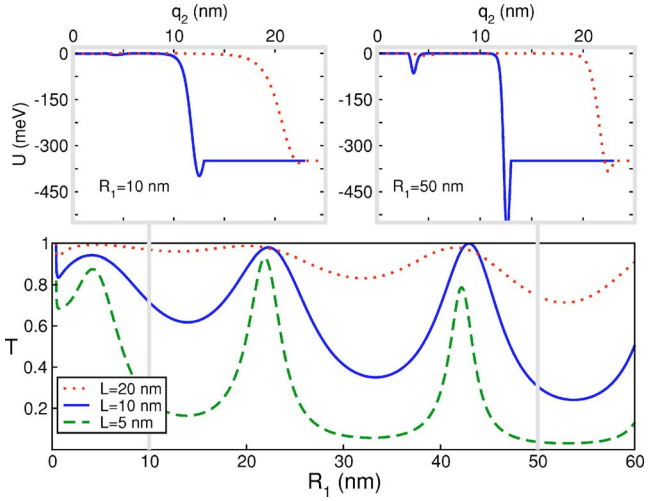

FIG. 8. (Color online) Transmission coefficient T for three single-junction structures with different L, as a function of R_1 (see Fig. 5), for $E_l=5$ meV and $R_2=0.397$ nm. The effective potential $U(q_2)$ is shown in the insets for two values of R_1 and two junction lengths, $L=10$ nm (solid line) and $L=20$ nm (dotted line). In both cases, the junction starts at $q_2=3$ nm.

resentative of the transmission properties within such structures.

The electron-transmission coefficient T for a single junction, as a function of the injection energy, is reported in Fig. 7. The electron comes from the cylinder with radius R_1 and is either reflected or transmitted to the cylinder with radius $R_2 \leqslant R_1$. The numerical analysis has been carried out for three different values of R_1, keeping R_2 and the junction length L fixed (see caption of Fig. 7). As in Sec. III, a single mass has been adopted in the numerical simulation in order to consider only the topological effects: the adopted effective mass corresponds to that of a nanotube with radius $R_2=0.397$ nm, i.e., of a (10,0) CNT. In the case $R_1 \sim R_2$ the transmission coefficient of the junction increases monotonically and is nearly unity for energies above 30 meV. In contrast, when R_1 is significantly different from R_2, T exhibits pronounced oscillations originating from in-resonance and off-resonance conditions. Furthermore, the average transmission coefficient decreases as R_1/R_2 increases. In order to investigate the effect of the junction geometry and to better understand the origin of the transmission characteristics, T has been computed, at a fixed value of the injection energy, as a function of the radius R_1 for three different junction lengths L. The results are shown in Fig. 8. It is easily seen that for a fixed R_1 a smaller L yields a lower transmission coefficient. In fact, the surface curvature in the connecting region is larger and, as a consequence, the potential U experienced by the electron along the structure is steeper (see top insets of Fig. 8). As expected, for a larger L (as in the case $L=20$ nm, dotted line in Fig. 8) the potential U is smoother and the resonance peaks of T are less pronounced. In general, for fixed values of R_1, R_2, and L, the shape of the function $\rho(q_2)$ determines that of U because, as shown in Eq. (20), the effective potential U depends on the local value of $\rho(q_2)$ and of its first and second derivatives. For instance, the two narrow dips at the junction ends, visible in the insets of Figs. 7 and 8, give a significant contribution to the resonance pattern, which adds to the contribution of the potential's slope. Such dips are more pronounced when the local curvature is larger, i.e., when the ratio R_1/R_2 is larger and/or L is smaller.

As indicated before, the five-degree polynomial of Eq. (15) is the lowest-order polynomial that guarantees a $\mathcal{C}^2$ regularity of the surface. Its second derivative is larger close to the junction ends, this originating the two dips in the effective potential. To check the influence of the shape of the connecting region we repeated the calculation of T with different forms of $\rho(q_2)$. We found that other forms providing a smooth transition from R_1 to R_2, similar to that analyzed above, do not modify significantly the transmission characteristics, as long as the surface of the connecting region is at least $\mathcal{C}^1$. An example of this result has recently been given in Ref. 21, where a double-parabola was used instead of the five-degree polynomial. A further decrease to $\mathcal{C}^0$ in the regularity of $\rho(q_2)$ would lead to the appearance of a Dirac's δ within the effective potential at each connecting point. This case has not been tackled.

In Fig. 8 it is apparent that the positions of the maxima of T are almost independent of L. However, such a result has been found to hold only when $R_1 > L$. A possible explanation is that, when the ratio R_1/L increases while R_2 is kept fixed, the coefficients F, G, U, ρ^{-2} of Eq. (23) reach a limiting form which introduces some periodicity into the solution. However, the correctness of this guess could not be checked so far, because an even approximate analytical solution is quite hard to work out for the problem at hand.

As far as the double junction structure (Fig. 6) is concerned, the transmission coefficient as a function of the in-

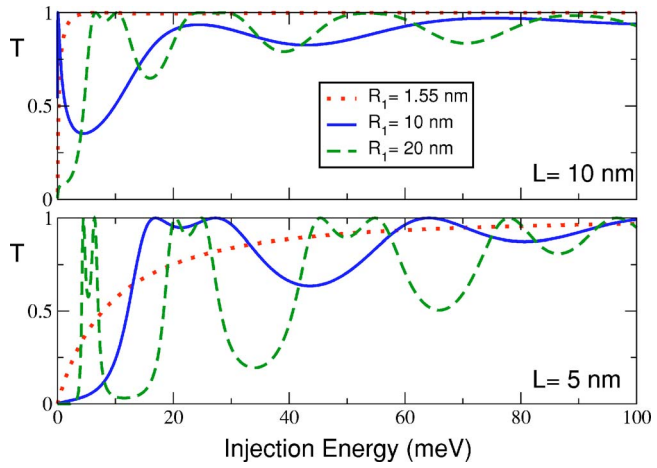

FIG. 9. (Color online) Transmission coefficient T for three double-junction structures with different R_1, namely $R_1=1.55$ nm (dotted line), $R_1=10$ nm (solid line), and $R_1=20$ nm (dashed line). The radius and length of the inner cylinder are fixed to $R_2=0.397$ nm and $D=5$ nm, respectively. Two different cases are reported, corresponding to $L=5$ and 10 nm.

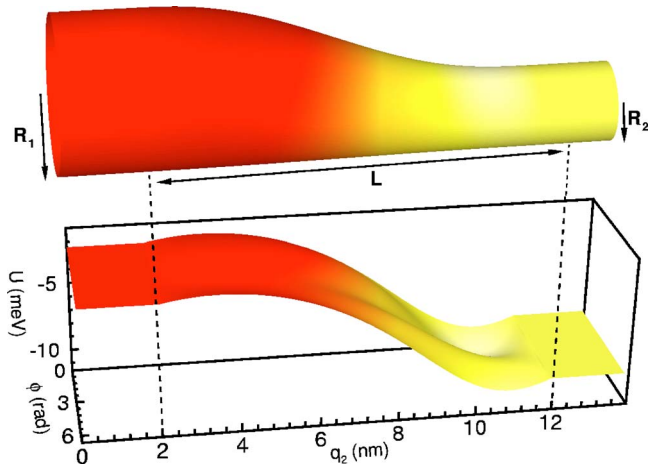

FIG. 10. (Color online) Asymmetric single junction. Top: 3D representation of the surface. The gray intensity shows the effective potential U as given by Eq. (28). Bottom: the effective potential as a function of the curvilinear coordinates (ϕ,q_2). Due to the asymmetry of the junction, the potential U depends on both ϕ and q_2.

jected electron energy is reported in Fig. 9. Results for three different radii R_1 and two different lengths L of the connecting regions are shown, while the length D of the inner cylinder and its radius R_2 have been kept fixed (the value of the other parameters are reported in the caption of Fig. 9). As before, a single effective mass corresponding to that of a (10,0) CNT has been adopted. The behavior of T is similar to that observed for a single junction: when the two radii are of the same order of magnitude, the surface curvature and the potential U are smooth and the transmission coefficient increases monotonically with E_l. Instead, for larger R_1/R_2, T becomes oscillatory and gives rise to resonance peaks. The oscillations have a more complicated structure with respect to the single junction case, due to the fact that the surface has four high curvature regions corresponding to four narrow wells in the potential U, which make the resonance conditions more complicated. This behavior is more evident when the length L of the connecting regions is shorter, since the surface curvature, and correspondingly the effective potential, becomes steeper.

V. ASYMMETRIC CYLINDRICAL JUNCTIONS

One of the most interesting curved surfaces is that shown in Fig. 10, made of the junction between two cylinders with different radii, whose axes are parallel but not coinciding. In fact, many images of junctions between two CNTs with different chiralities have been reported in the literature, showing that the larger-diameter CNT joins the smaller-diameter one through a section containing a single pentagon and a single heptagon at the edges of the junction.[22,23] In this section, the transmission properties of such a surface are addressed and compared to the symmetric-junction case.

The asymmetric cylindrical junction S_{acj} is given by the following parametric equations:

$$x = \rho(q_2)\cos\phi,$$

$$y = q_2,$$

$$z = \rho(q_2)\sin\phi + \rho(q_2) - R_1, \tag{26}$$

where $\rho(q_2)$ is the q_2-dependent radius of the cylinder and (ϕ,q_2) are the curvilinear coordinates. As described above, the asymmetry comes from the fact that, as the radius of the cylinder changes from R_1 to R_2, the center of the circular section changes as well, as shown in the top part of Fig. 10. This topology mimics the one experimentally observed for CNT junctions, as indicated at the beginning of this section. As for the junctions with axial symmetry, the shape of $\rho(q_2)$ has been modeled with a five degree polynomial [see Eq. (15)]. The case of a single asymmetric junction is analyzed here and compared to the symmetric one.

The first and second fundamental forms are

$$\mathbf{G} = \begin{pmatrix} \rho(q_2)^2 & \rho(q_2)\rho'(q_2)\cos\phi \\ \rho(q_2)\rho'(q_2)\cos\phi & 1 + 2\{\rho'(q_2)\}^2[1+\sin\phi] \end{pmatrix},$$

$$\mathbf{H} = \frac{1}{\sqrt{1+\{\rho'(q_2)\}^2[1+\sin\phi]^2}} \times \begin{pmatrix} \rho(q_2) & 0 \\ 0 & -\rho''(q_2)[1+\sin\phi] \end{pmatrix}, \tag{27}$$

where the single- and double-prime superscripts indicate the first and second derivative, respectively. The effective potential U reads

$$U(q_2,\phi) = -\frac{\hbar^2}{2m}\left\{\frac{[1+(1+\sin\phi)(2\rho'^2-\rho\rho'')]^2}{4\rho^2[1+\rho'^2(1+\sin\phi)^2]^3} + \frac{\rho''(1+\sin\phi)}{\rho[1+\rho'^2(1+\sin\phi)^2]^2}\right\}, \quad (28)$$

where the dependency of the radius ρ on the coordinate q_2 has been omitted for the sake of conciseness. In contrast to the symmetric junctions, in this case the first and second fundamental forms, as well as the effective potential U, are not separable with respect to the curvilinear coordinates. As a consequence the Hamiltonian, whose expression is given by the general form (1), must be solved by means of a fully 2D simulation. As in the previous cases, the ground state of the angular part has been taken for the incident wave function but, due to the nonseparability, higher angular modes arise in the transmitted and reflected components. We describe, in the following, the mechanism leading to the transmission characteristics by considering the specific geometrical parameters used in our simulations. The electron is injected into the cylinder with larger radius R_1, that takes the values 1.55, 5, and 10 nm in the numerical simulations. The energy spacing between the angular modes of the incoming cylinder is smaller than that of the outgoing cylinder. In the latter, the radius is fixed to $R_2=0.397$ nm which, in turn, provides an energy difference between the ground and first excited angular states of about 1.4 eV. Let $U_1=-\hbar^2/(8mR_1^2)$ and $U_2=-\hbar^2/(8mR_2^2)$ be the constant effective potential of the incoming and outgoing cylinders, respectively: for the junctions analyzed here, U_1-U_2 is about 350 meV. As a consequence, only electrons injected with a total energy $E>1.05$ eV can be transmitted in angular modes other than the ground state. For increasing E, the number of available channels for the reflection in the incoming cylinder increases, while only one transmission channel is available up to $E=1.05$ eV. This influences the behavior of the transmission coefficient T, which is shown in Fig. 11 as a function of the injection energy E_l for three different radii R_1. In the case $R_1 \sim R_2$, the transmission coefficient increases monotonically until the number of angular channels in the incoming cylinder changes from 1 (ground state) to 3 (ground state plus double-degenerate first excited state): for $R_1=1.55$ nm, this happens when $E_l \sim 90$ meV, where T begins to decrease, showing a sharp lowering when the new incoming angular modes arise. The same behavior can be observed for the higher R_1 values, where the transmission coefficient shows a number of sharp lowerings corresponding to the appearance of new angular channels in the incoming cylinder (see, for examples, the curve $R_1=10$ nm at $E_l \simeq 20$, 35, and 53 meV). When the total energy $E=E_l+U_1$ reaches 1.05 eV, new modes arise in the outgoing cylinder: this results in a sharp increase of T, as can be seen in the inset of Fig. 11, where the transmission coefficient is shown for injection energies up to 2 eV for $R_1=1.55$ nm. After the appearance of the new outgoing-cylinder angular modes and the corresponding sharp increase of T, the transmission coefficient decreases for increasing injection energies. This happens because, as already described above, new angular modes for reflection continue to become available, while those for transmission

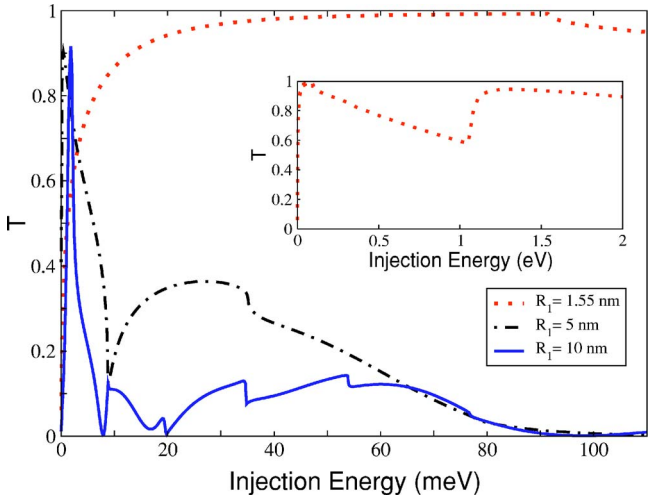

FIG. 11. (Color online) Transmission coefficient T as a function of injection energy E_l for an asymmetric junction. Three cases are reported, corresponding to $R_1=1.55$ nm (dotted line), $R_1=5$ nm (dotted-dashed line), and $R_1=10$ nm (solid line), with R_2 and L fixed to 0.397 and 5 nm, respectively. Inset: the transmission coefficient for the case $R_1=1.55$ nm is plotted for an injection energy ranging from 0 to 2 eV.

remain unchanged. A comparison between Figs. 11 and 7 shows that the nonseparability of the asymmetric junction leads to a totally different behavior of the transmission coefficient with respect to that obtained for a symmetric cylindrical junction with the same geometrical parameters. In particular we note that in the case under analysis, and in contrast to the separable case analyzed in Sec. IV, T globally decreases at higher energies. In fact, the density of the angular channels is higher in the injection/reflection cylinder (with larger radius) than in the outgoing cylinder. In turn, the 2D potential makes the wave function to become a superposition of angular modes that does not occur in the symmetric case. This indicates that the topology of the junction plays a substantial role in its coherent-transmission properties.

VI. LOCALIZED STATES

Two of the structures analyzed in the previous sections, namely, the bent cylinder and the double junction, are characterized by an effective potential U that forms a well, whose depth and shape depends on the geometrical parameters (see, e.g., Figs. 2 and 6). As a consequence these kinds of structures are able to bind carriers in the quantum states localized within the well. In the analysis carried out so far, the localized states were assumed unoccupied. If this were not the case, the transmission characteristics would strongly be modified by the Coulomb interaction between the propagating electron and the bound one. The analysis of the carrier-carrier interaction is beyond the scope of this work, where only the single-particle dynamics has been addressed.

The energy spectra of the localized states have been computed for both structures in order to analyze their dependency on the geometrical parameters. In the bent-cylinder case, one finds that only one localized state is present for the

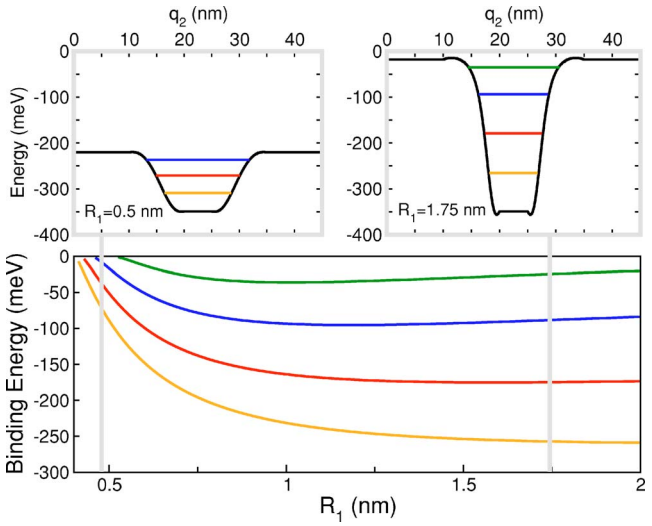

FIG. 12. (Color online) Binding energy, as a function of the radius R_1, of the electron states localized in the central cylinder of a double junction. The geometrical parameters are $L=10$ nm, $D=5$ nm, and $R_2=0.397$ nm. The number of bound states increases from 1 to 4 as R_1 ranges from 0.4 nm (i.e., around the value of R_2) to 2 nm.

geometrical configurations we adopted in the investigation of the transmission coefficient. The amplitude of the wave function corresponding to the bound state is maximal on the "inner" side of the structure. For a fixed cylinder radius ρ, the absolute value of the binding energy increases for an increasing curvature angle θ because the length of the well increases (see Figs. 1 and 2), and/or a decreasing curvature radius R because the depth of the well increases. For the analyzed structures the calculated binding energies are in the meV range. As an example, for a bent cylinder with $R=2$ nm, $\rho=1.55$ nm, and $\theta=\pi/2$ the binding energy is -4 meV. It is worth observing that in the cases considered here the binding energy is relatively small with respect to the injection energy of a propagating electron. As a consequence it can realistically be assumed that a localized electron would easily be scattered away.

In the double-junction a number of localized states are present in the smaller-radius cylinder, where the surface curvature creates a potential well (Fig. 6). The calculated binding energies are reported in Fig. 12. As R_1 increases, the effective potential well becomes narrower in average and deeper, as shown in the insets of Fig. 12. The change in width and depth influences the energy spectrum depending on the range of R_1. In particular, for R_1 values up to 0.8 nm the binding energies decrease with increasing R_1, and new bound states are created as the well deepens. At higher R_1 values, the depth of the well changes slightly since U saturates to the flat-surface value in a way similar to that of the bent cylinder discussed in Sec. III, and the effect of the well narrowing becomes more relevant. As a consequence, the binding energies of the states increase as shown in Fig. 12. In the double junction the localized states are in general more strongly bound than in the bent cylinder, but it is readily verified that the Coulomb blockade inhibits a double occupancy of such states.

VII. CONCLUSIONS

In this work, the analysis of quantum states and coherent dynamics of a particle bound to a surface has been performed using a mixed analytical-numerical approach. In particular, the case of cylindrical surfaces has been addressed and the transmission coefficient has been calculated for surface states of bent cylinders and cylindrical junctions, in order to capture the main coherent-transport features related to their geometrical shape. To this purpose, a 2D open-boundary numerical solver has been developed for the solution of the coherent dynamics of a particle strongly bound to a surface, based on the assumption that the degree of freedom corresponding to the direction orthogonal to the surface can be ruled out. This leads to a 2D Schrödinger-like dynamic equation with an additional potential U depending on the local curvature of the surface. We showed how the latter potential is able to strongly influence the quantum transmission characteristics of the structures under investigation.

In the case of bent cylinders the transmission coefficient T is found to significantly differ from unity at low injection energies and for a steep bending. In the case of cylindrical junctions, T is affected by the shape of the connecting region: in particular, it increases with the injection energy for a junction with axial symmetry, while it decreases in the case of asymmetric junctions. We believe that this topological effect, that has a purely quantum-mechanical origin, must be taken into account when modeling charge transport phenomena in a 2D domain bent within the 3D space, as, for example, in an effective-mass description of a bent CNT.

Another effect of the surface bending is the formation of localized states. We found that particles can be strongly bound to the surface states of a double cylindrical junction in case the radius of the inner cylinder is substantially smaller (around one half or less) than that of the outer cylinders. On the other hand, in a bent cylinder a single localized state is present. It is always weakly bound (few meV in the analyzed geometries) and the probability of localizing the particle is higher in the "inner" part of the bending (toward the curvature center). We note that, since the potential U is originated only by the surface topology, it will affect positively and negatively charged carriers in an identical manner.

The approach described so far not only represents an instrument for the basic investigation of the transmission characteristics of quantum states confined on a bent surface, but can also be an efficient means to include the geometrical effects originated by the shape of CNTs and CNT junctions, provided that the inclusion of a realistic band structure or a proper position-dependent effective mass allows one to take into account the electronic properties originated by the lattice periodicity.

*Electronic address: amarchi@deis.unibo.it

[1] S. J. Tans, A. R. M. Verschueren, and C. Dekker, Nature (London) **393**, 49 (1998).
[2] A. Marchi, A. Bertoni, S. Reggiani, and M. Rudan, IEEE Trans. Nanotechnol. **3**, 129 (2004).
[3] R. Folman, P. Krüger, D. Cassettari, B. Hessmo, T. Maier, and J. Schmiedmayer, Phys. Rev. Lett. **84**, 4749 (2000).
[4] R. C. T. da Costa, Phys. Rev. A **23**, 1982 (1981).
[5] H. Aoki, M. Koshino, D. Takeda, H. Morise, and K. Kuroki, Phys. Rev. B **65**, 035102 (2002).
[6] G. Cantele, D. Ninno, and G. Iadonisi, Phys. Rev. B **61**, 13730 (2000).
[7] I. V. Blonskyy, V. M. Kadan, A. K. Kadashchuk, A. Y. Vakhnin, A. Y. Zhugayevych, and I. V. Chervak, Phys. Low-Dimens. Struct. **7–8**, 25 (2003).
[8] For an overview of the experimental characterization and theoretical modeling of porous silicon, see O. Bisi, S. Ossicini, and L. Pavesi, Surf. Sci. Rep. **38**, 1 (2000).
[9] N. Hurt, *Mathematical Physics of Quantum Wires and Devices: From Spectral Resonances to Anderson Localization*, Vol. 506 of *Mathematics and its Applications* (Kluwer, Dordrecht, 2000).
[10] R. Saito, G. Dresselhaus, and M. S. Dresselhaus, *Physical Properties of Carbon Nanotubes* (Imperial College Press, London, UK, 1998).
[11] R. Saito, M. Fujita, G. Dresselhaus, and M. S. Dresselhaus, Phys. Rev. B **46**, 1804 (1992).
[12] L. C. Venema, J. W. Janssen, M. R. Buitelaar, J. W. G. Wildöer, S. G. Lemay, L. P. Kouwenhoven, and C. Dekker, Phys. Rev. B **62**, 5238 (2000).
[13] A. Rochefort, D. Salahub, and P. Avouris, Chem. Phys. Lett. **297**, 45 (1998).
[14] M. V. Fischetti and S. E. Laux, Phys. Rev. B **48**, 2244 (1993).
[15] G. L. Zhao, D. Bagayoko, and L. Yang, Phys. Rev. B **69**, 245416 (2004).
[16] G. Pennington and N. Goldsman, in *Proceedings of the SISPAD Conference*, edited by D. Tsoukalas and C. Tsamis (Springer, New York, 2001), pp. 218–221.
[17] D. J. Struik, *Differential Geometry* (Addison-Wesley, Cambridge, 1950).
[18] C. S. Lent and D. J. Kirkner, J. Appl. Phys. **67**, 6353 (1990).
[19] P. Ordejón, E. Artacho, and J. M. Soler, Phys. Rev. B **53**, R10441 (1996).
[20] D. Sánchez-Portal, E. Artacho, and J. M. Soler, Int. J. Quantum Chem. **65**, 453 (1997).
[21] A. Marchi, A. Bertoni, S. Reggiani, and M. Rudan, in *Proceedings of the IEEE Conference on Nanotechnology* (IEEE, New York, 2004), pp. 104–106.
[22] S. Iijima, T. Ichihashi, and Y. Ando, Nature (London) **356**, 776 (1992).
[23] M. Endo, K. Takeuchi, K. Kobori, K. Takahashi, H. W. Kroto, and A. Sarkar, Carbon **33**, 873 (1995).